IOP Publishing New J. Phys. 27 (2025) 033007 https://doi.org/10.1088/1367-2630/adb2b8

New Journal of Physics
The open access journal at the forefront of physics

Deutsche Physikalische Gesellschaft DPG
IOP Institute of Physics

Published in partnership with: Deutsche Physikalische Gesellschaft and the Institute of Physics

OPEN ACCESS

RECEIVED
21 December 2023

REVISED
26 November 2024

ACCEPTED FOR PUBLICATION
5 February 2025

PUBLISHED
3 March 2025

PAPER

Characterizing the magnetic noise power spectrum of dark spins in diamond

Ethan Q Williams* and **Chandrasekhar Ramanathan**

Department of Physics and Astronomy, Dartmouth College, Hanover, NH 03755, United States of America
* Author to whom any correspondence should be addressed.

E-mail: ethan.q.williams@dartmouth.edu and chandrasekhar.ramanathan@dartmouth.edu

Keywords: diamond, nitrogen vacancy, P1, electron spin paramagnetic resonance, dynamical decoupling, noise spectroscopy, quantum sensing

Supplementary material for this article is available online

Abstract

The coherence times of solid-state spin qubits are often limited by the presence of a spin bath. Characterizing the spectrum of the local magnetic field fluctuations of the bath is key to understanding spin qubit decoherence. Here we use pulsed electron paramagnetic resonance (pEPR) based noise spectroscopy to measure the magnetic noise power spectra for ensembles of substitutional nitrogen (P1) centers in diamond that typically form the bath for nitrogen-vacancy (NV) centers. The Carr–Purcell–Meiboom–Gill (CPMG) dynamical decoupling experiments on the P1 centers were performed on a low [N] chemical vapor deposition (CVD) sample and a high [N] high-temperature, high-pressure (HPHT) sample at 89 mT. We characterize the NV centers of the latter sample using the same 2.5 GHz pEPR spectrometer. All power spectra show two distinct features, a broad component that is observed to scale as approximately $1/\omega^{0.7-1.0}$, and a prominent peak at the ^{13}C Larmor frequency. The behavior of the broad component is consistent with an inhomogeneous distribution of Lorentzian spectra due to clustering of P1 centers, which has recently been shown to be prevalent in HPHT diamond. We develop techniques utilizing harmonics of the CPMG filter function to improve characterization of high-frequency signals, which we demonstrate on the ^{13}C nuclear Larmor frequency. At 190 mT this is 2.04 MHz, 5.7 times higher than the CPMG modulation frequency (<357 kHz, hardware-limited). Understanding the properties of the bath allow us to either exploit it as a quantum resource or optimize decoupling performance, while also informing sample fabrication technologies. The techniques are applicable to ac magnetometry for nanoscale nuclear magnetic resonance and chemical sensing.

1. Introduction

In solid-state spin systems, the magnetic fluctuations produced by other spins—both electronic and nuclear—in the system are often the main source of decoherence. For example, it is the interactions with ^{13}C nuclear spins and the electronic spins of substitutional nitrogen (P1) centers that dominate the magnetic fluctuations seen by nitrogen-vacancy (NV) centers in bulk diamond. However, in addition to being a source of decoherence, dark spins in diamond are also a promising platform for studying the many-body physics of interacting spin systems [1–3] and may themselves be used as qubits for quantum sensing and computation [4]. The ability to directly probe the properties of dark spins is key to helping understand the coherence properties of new spin qubit platforms based on molecular magnets [5, 6] and embedded radical systems [7–9].

Dynamical decoupling (DD) [10, 11] noise spectroscopy (NS) has become an important tool in characterizing qubit environments in different physical platforms [12–27]. Optically detected magnetic resonance (ODMR) has been used to characterize the magnetic noise fluctuations around both single NV centers and ensembles [28–42]. Additionally, double electron–electron resonance NV-P1 experiments have been used to probe the properties of the dark P1 spins via the NV centers [3, 40, 43, 44]. Here, we apply DD

NS to the dark spins directly using inductively-detected pulsed electron paramagnetic resonance (pEPR). We characterize the noise spectrum of ensembles of P1 centers in both a relatively low [N] CVD sample and a relatively high [N] high-temperature, high-pressure (HPHT) sample. We show that pEPR can also be used to characterize the noise spectrum of the NV centers in the HPHT sample, allowing us to compare our results to previous ODMR measurements. While typically performed on large ensembles of spins, inductive detection of small ensembles on the order of 1000 spins can also be performed [45, 46].

For diamond-based quantum sensing and information applications, nitrogen concentrations between approximately 1 ppm and 100 ppm play a non-trivial role in the spin coherence dynamics [47–49]. The T_2 of the NV center has been used to estimate the local P1 concentration via ensemble experiments on isotopically engineered chemical vapor deposition (CVD) diamond [48]. However, such scaling relationships need to be used carefully as the distribution of the P1 centers is not always uniform. For example, it has recently been shown that HPHT diamond with a reported nitrogen concentration of [N] $\approx$ 200 ppm that was irradiated and annealed for the creation of NV centers had local P1 concentrations varying as widely as 10–300 ppm [40]. Clustering of P1 spins in HPHT diamond has also been observed via high-field pEPR [50, 51] and gives rise to multiple mechanisms for dynamic nuclear polarization [52].

We extend standard DD NS analysis techniques to reconstruct the magnetic noise power spectra seen by the P1 spins in both the HPHT and CVD samples and the NV spins in the HPHT sample. All power spectra showed two distinct features, a broad component that is observed to scale as approximately $1/\omega^{0.7-1.0}$, and a prominent peak at the ^{13}C Larmor frequency. We also develop techniques that utilize the higher harmonics of the Carr–Purcell–Meiboom–Gill (CPMG [10, 11]) filter function to improve our ability to characterize peaks in the power spectrum at frequencies higher than the CPMG maximum modulation frequency (about 360 kHz with our hardware). Note that Goldblatt *et al* observed coherent P1-^{13}C interactions at low field (from 4 mT to 10 mT) on a sample with [N] $\approx$ 1 ppm [3]. The experiments shown here probe both low and high [N] samples at higher magnetic fields.

2. Experiment overview

The experiments are performed on a 2.5 GHz lab-built pEPR spectrometer. We can access 3 resonance configurations at this frequency. For the negatively charged spin-1 NV center, the $|0\rangle \leftrightarrow |-1\rangle$ resonance frequency crosses 2.5 GHz at $B_0 = 13$ mT and 190 mT. For the spin-1/2 P1 center the $|-1/2\rangle \leftrightarrow |1/2\rangle$ resonance occurs at 89 mT. For both P1 and NV centers, hyperfine interactions with the host ^{14}N nucleus (spin-1), result in three nuclear spin manifolds, and we set our magnetic field such that our pulses are on resonance with the central ($m_I = 0$) manifold.

A cartoon of the spin environment in diamond is shown in figure 1(a). There are two diamond samples used in this work, both purchased from Element 6. Sample A is a HPHT Type Ib diamond with a stone-type cut, approximate dimensions $4.2 \times 5.7 \times 1.3$ mm^3, and nitrogen and NV concentrations measured to be [N] = 87(8) ppm and [NV] = 1.7(3) ppm. Sample B is a CVD diamond plate with approximate dimensions $3.25 \times 3.17 \times 0.28$ mm^3 and [N] = 0.39(9) ppm. A full description of the samples is given in supplementary information S1.

A schematic of the CPMG sequence is shown in figure 1(b). In a single CPMG experiment with a fixed pulse-spacing τ, we stroboscopically acquire each echo formed. Figure 1(d) shows examples of time traces of single echoes from the four spin species addressed in this work, while figure 1(e) shows example CPMG decay envelopes.

The microwave excitation and detection is performed inductively using a loop-gap resonator [53–55]. We use a capacitive antenna coupling to the resonator which houses the diamond sample as depicted in figure 1(c). Details of the experimental setup are provided in supplementary information S3.

2.1. P1 centers

In the P1 center, the ^{14}N hyperfine interactions are strong, and the $m_I = +1$ or -1 resonance lines are outside the bandwidth of the pEPR pulse. A Jahn–Teller distortion can generate up to 4 spectral lines for each state m_I of the host nitrogen [44, 56]. For the P1 experiments on Sample A (B), the sample is oriented with the [111] ([100]) axis aligned with $\vec{B}_0$. For both sample alignments, the 4 spectral lines of the $m_I = 0$ manifold spectrally overlap and are indistinguishable as evidenced by echo-detected field sweep spectra shown in supplementary information S2.

P1 CPMG data for Sample A (B) was acquired with 16 384 (65 536) repetitions for averaging. High amounts of averaging are required to obtain sufficient signal-to-noise due to the low thermal spin polarization. At $T = 300$K the thermal spin polarization of the P1 centers is $\epsilon_{\text{th}} \approx 2.0 \times 10^{-4}$.

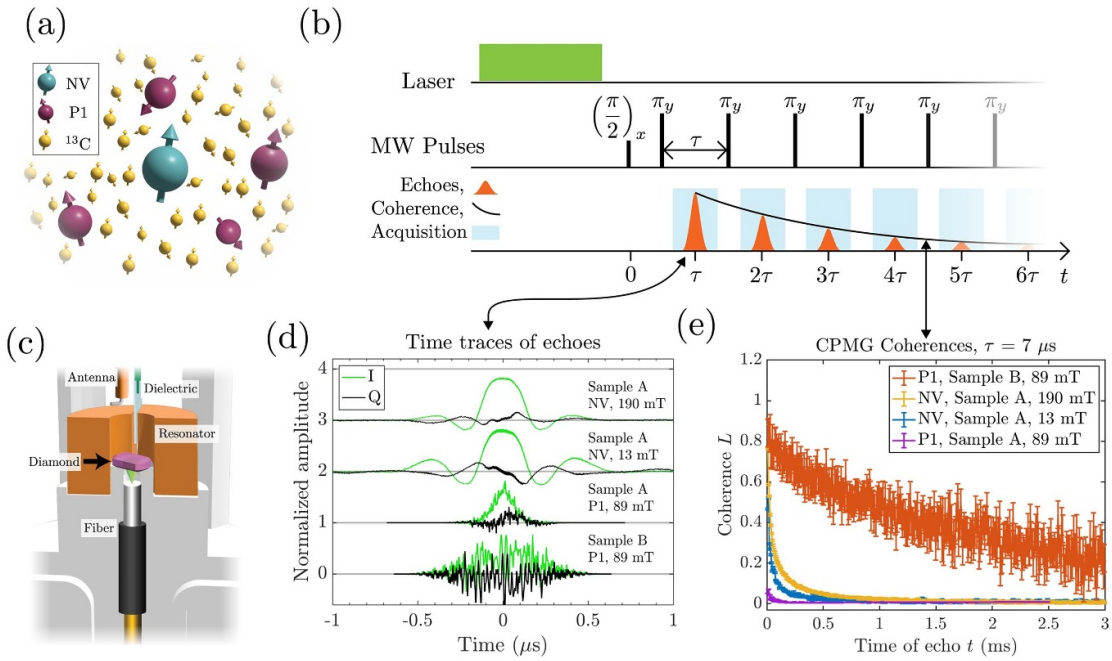

Figure 1. (a) Cartoon of the central spin model, depicting the NV center as the central spin of a disordered system. (b) Schematic of the CPMG experiment protocol. The laser is used only for NV experiments. The Nth echo occurs at detection time $t = N\tau$. In a single shot, we acquire each echo that forms until the signal has diminished below the noise floor. The decay of the echo amplitudes is represented by the coherence curve. (c) Illustration of the assembly of the diamond sample, loop-gap resonator (cutaway view), optical fiber (emitting green 532 nm light), microwave antenna, and sapphire dielectric used for tuning the resonator. (d) Example time traces of spin echo for each of the spin species targeted in this work. For each time trace, the in-phase and quadrature ('I' and 'Q') components are shown. Sample A is the HPHT diamond and Sample B is the CVD diamond. (e) Examples of CPMG coherence decays with fixed $\tau = 7$ μs.

2.2. NV centers

For the NV experiments, Sample A is oriented so that the [111] axis is aligned with $\vec{B}_0$. Here, the three hyperfine lines are within the bandwidth of our ∼50 ns microwave pulse as evidenced by the echoes and spectra in figures S2 and S3 of supplementary information S2. The NV centers in the diamond sample are initialized to the $|m_s\rangle = |0\rangle$ ground state with a 10 ms pulse of 532 nm unfocused light transmitted via an optical fiber. The intensity of the light incident on the diamond is 1 W mm^{-2} and directly illuminates approximately 1/3 of the sample, while the light that is reflected and diffused by the sample and sample holders illuminates the rest. The mean hyperpolarization with green light, calculated from the observed signal enhancement, is $\epsilon_{\text{hyp}} \approx 120\epsilon_{\text{th}}$. As a result only 128 repetitions were needed for the NV center experiments.

3. DD-based spectroscopy in diamond

3.1. System and decoherence model in diamond

For the NV spins in Sample A and P1 spins in Sample B the concentration of the measured spins is low and the dipolar interactions between identical measured spins can be ignored. In these cases the underlying physics for both systems can be described in terms of the central spin model [57]. Here the environment consists of a spin bath as we can ignore interactions with lattice phonons on timescales shorter than the spin-lattice relaxation time T_1. Note, however, this model breaks down when considering the P1 spins in Sample A, where dipolar interactions between the P1 spins can no longer be ignored.

For an electronic central spin in diamond (in the $m_I = 0$ ^{14}N manifold), the total Hamiltonian can be expressed as

$$H_{\text{Tot}}(t) = H_{\text{S}} + H_{\text{C}}(t) + H_{\text{E}} + H_{\text{SE}} \tag{1}$$

where H_{S}, the system Hamiltonian, determines the effective resonance frequency of the system under study and so contains the Zeeman interaction with the external magnetic field, and, in the case of the NV center, the zero-field splitting. The control Hamiltonian is $H_{\text{C}}(t) = -\gamma_e \vec{S} \cdot \vec{B}_1(t)$, where $\vec{S}$ is the central spin operator vector (S_x, S_y, S_z) and $\vec{B}_1(t)$ is the magnetic microwave control field. The environment Hamiltonian H_{E} consists of the Zeeman and spin-spin interactions for bath spins in the vicinity of the central spin. The

system-environment Hamiltonian $H_{\rm SE}$ includes the interactions between the central spin and the bath spins. The bath consists of ^{13}C nuclear spins, and unlike electron spins. When the NV is the central spin, the unlike electron spins are the P1 spins. When the P1 is the central spin the unlike electron spins are P1 spins of spectrally-separated ^{14}N hyperfine manifolds. Since the experiments on the P1 centers in Sample B are performed on the $m_I = 0$ hyperfine manifold, the unlike electrons that constitute the bath are those in the $m_I = \pm 1$ states.

For a well-quantized central spin (along z), the system-environment Hamiltonian is

$$H_{\rm SE} = S_z \left[\sum_i \left(A^i_\perp I^i_x + A^i_\parallel I^i_z \right) + \sum_i J^i_\parallel S^i_z \right]. \tag{2}$$

The first summation in the brackets is over the nuclear spins, where $A^i_\perp$ and $A^i_\parallel$ are the transverse and longitudinal hyperfine coupling components between the central spin and the ith ^{13}C nuclear spin (with spin operators I^i_x and I^i_z). The second summation is over the unlike electron spins in the central spin's environment. $J^i_\parallel$ is the coupling strength between the central spin and the S^i_z component for the ith unlike electron spin. The transverse components of the electron–electron coupling are non-secular and thus omitted.

In the interaction frame defined by the system and environment Hamiltonians ($H_{\rm S} + H_{\rm E}$), the system-environment Hamiltonian $H_{\rm SE}$ becomes time-dependent. The system dynamics are approximately generated by an effective central spin Hamiltonian [57]:

$$H^{(E)}_{\rm SE}(t) = -\gamma_e b_z(t) S_z \,, \tag{3}$$

where $b_z(t)$ is the z-component of the time-varying magnetic field noise at the site of the central spin. It is the sum of the magnetic fields produced by the fluctuating environment spins and contains periodic components at the ^{13}C Larmor frequency.

For the denser P1 centers in Sample A, the system Hamiltonian in equation (1) also includes dipolar couplings between P1 centers within the same $m_I = 0$ manifold. As a result the effective 'noise' seen by a single P1 center will no longer look like an effective classical field as described by equation (3). Thus, while we can still perform the analysis along the lines described below, the results need to be interpreted more carefully.

3.2. The CPMG experiment and NS

The application of a π-pulse flips the sign of $H^{(E)}_{\rm SE}$ of equation (3) in a toggling frame representation. For DD sequences, which consist of a train of π pulses, the repeated flipping of the sign can be expressed by a square-wave frame modulation function $f_z(t,\tau)$ [12, 14, 16, 21]. The effective toggling frame Hamiltonian for the dephasing noise acting on the central spin under application of DD is expressed as

$$\tilde{H}_{\rm SE}(t,\tau) = -\gamma_e f_z(t,\tau) b_z(t) S_z. \tag{4}$$

In the CPMG sequence, a series of π_y pulses is applied such that the Nth π_y pulse occurs at time $t_N = \tau(N - 1/2)$ and the Nth echo is detected at time $t = N\tau$. The amplitude of the Nth echo is given by the expectation value for S_y:

$$\langle S_y(t,\tau)\rangle = -\frac{\epsilon}{2}\cos(\phi(t,\tau)) \tag{5}$$

where $\phi(t,\tau)S_z = \int_0^t {\rm d}t' \tilde{H}_{\rm SE}(t',\tau)$. The coherence $L(t,\tau)$ is given by the normalized ensemble average of S_y:

$$L(t,\tau) = \frac{\langle S_y(t,\tau)\rangle_{\rm ens}}{\langle S_y(0,\tau)\rangle_{\rm ens}} = \langle \cos(\phi(t,\tau))\rangle_{\rm ens}. \tag{6}$$

For a disordered system composed of many weak couplings to the central spin, it is useful to make the approximation that $b_z(t)$ is drawn from a stationary Gaussian random distribution with zero mean. Then $\phi(t,\tau)$ for the ensemble is a Gaussian random variable [57]. In this case, the coherence can be shown to be $L(t,\tau) = {\rm e}^{-\langle\phi(t,\tau)^2\rangle/2}$, where $\langle\phi(t,\tau)^2\rangle$ is the variance of the ensemble phase distribution. We set $\langle\phi(t,\tau)^2\rangle/2 = \chi(t,\tau)$ such that the coherence can simply be expressed as $L(t,\tau) = {\rm e}^{-\chi(t,\tau)}$.

The quantity χ can be expressed in terms of a dimensionless filter function $F(\omega,t,\tau)$ and the power spectral density $S(\omega)$ of the magnetic noise $b_z(t)$.

$$\chi(t,\tau) = \frac{t^2}{2}\int_{-\infty}^{\infty} {\rm d}\omega\, S(\omega) F(\omega,t,\tau). \tag{7}$$

The filter function $F(\omega, t, \tau)$ of the DD sequence is

$$F(\omega, t, \tau) = \frac{1}{t^2}\left|\frac{1}{\sqrt{2\pi}}\int_0^t f_z(t', \tau)\, e^{-i\omega t'}\, dt'\right|^2, \tag{8}$$

and the power spectral density $S(\omega)$ is the Fourier transform of $g(t') = \gamma_e^2\langle b_z(\tilde{t}) b_z(\tilde{t}+t')\rangle$, the autocorrelation function of $b_z(t)$

$$S(\omega) = \frac{1}{\sqrt{2\pi}}\int_{-\infty}^{\infty} g(t')\, e^{-i\omega t'}\, dt'. \tag{9}$$

The challenge of NS is to calculate $S(\omega)$, given the measured χ values and the form of the filter F that describes the control sequence. In the large N limit of instantaneous π pulses, the filter function can be approximated as the sum of δ-functions

$$F(\omega, t, \tau) \approx \frac{4}{t\tau^2}\sum_{m=\pm\text{odd}}^{\infty}\frac{\delta(\omega - m\pi/\tau)}{\omega^2}. \tag{10}$$

which results in a discrete sum expression for χ:

$$\chi(t, \tau) = \frac{4t}{\pi^2}\sum_{m=1,3,5,\ldots}^{\infty}\frac{S(\omega_m)}{m^2}, \tag{11}$$

where $\omega_m = m\pi/\tau$. If $S(\omega_1) \gg S(\omega_m)$ for all $m > 1$, it is appropriate to approximate F as a single peak at the fundamental ($m = 1$) frequency $\omega = \pi/\tau$ and ignore the contributions of higher harmonics,

$$S(\omega) = S(\omega_1) = \frac{\pi^2\,\chi(t, \tau)}{4t}. \tag{12}$$

For a smooth spectrum that monotonically decays with ω, a sequence with a shorter τ value decouples the system from a greater range of low-frequency noise and therefore extends coherence more than a sequence with a longer τ value does. However, if a peak in the filter function F overlaps with a sharp peak in the power spectrum S, this will cause a sharp dip in the coherence. Equivalently, if $\tau = mT/2$ ($m = 1, 3, 5\ldots$), where T is the oscillatory period of a prominent noise source, such as the ^{13}C Larmor precession, then the coherence decays much more quickly than it otherwise would. This sensitivity is the key to AC magnetometry.

4. Results and discussion

4.1. Overview of data

The observed coherence decay is a product of the decay due to spin bath interactions and, to a lesser extent, T_1 relaxation, $L_{\text{obs}}(t) = \exp[-(t/(2T_1) - \chi(t)]$. In the absence of a spin bath, we expect that the T_2 relaxation would be dominated by spin-lattice interactions and $T_2 = 2T_1$. Accordingly, to correct for the effects of T_1 relaxation, such that χ only reflects decoherence due to the bath spins, we calculate χ as

$$\chi(t) = -\log(L_{\text{obs}}(t)) - \frac{t}{2T_1}. \tag{13}$$

The measured T_1 times are on the order of milliseconds and have little effect on the NV χ calculation, for which the coherence times are on the order of 100 μs. The T_1 correction is slightly more significant for the P1 center data in Sample B, which achieves coherence times around $T_1/2$ in the short τ limit. Details of T_1 and T_2 experiments and the resulting values are provided in supplementary information S1.

Figure 2 shows image plots of χ data with the T_1-correction of equation (13) for the NV center experiments at 13 mT and 190 mT ((a) and (b)), and P1 center experiments at 89 mT on the CVD and HPHT diamond samples ((c) and (d)). The vertical axes of the image plots indicate the time at which an echo occurs. Therefore, a single-shot experiment with fixed τ is represented by a vertical line ascending from bottom to top of the image plot. As the echo amplitudes decay, L decreases from 1 to the noise floor, as limited by the signal-to-noise of the experiment, and χ increases from 0 to some χ_{max}, which is about 5.5 for the Sample A NV datasets, 5.2 for the Sample A P1 dataset, and about 3.5 for the Sample B P1 dataset. In the lower right areas of the figure 2 image plots, one can see sections of data that are uniform in the vertical direction, and the boundaries of the sections are slanted from lower left to upper right. This is because each section corresponds to a particular echo number N. The lower rightmost section appears almost as a triangle,

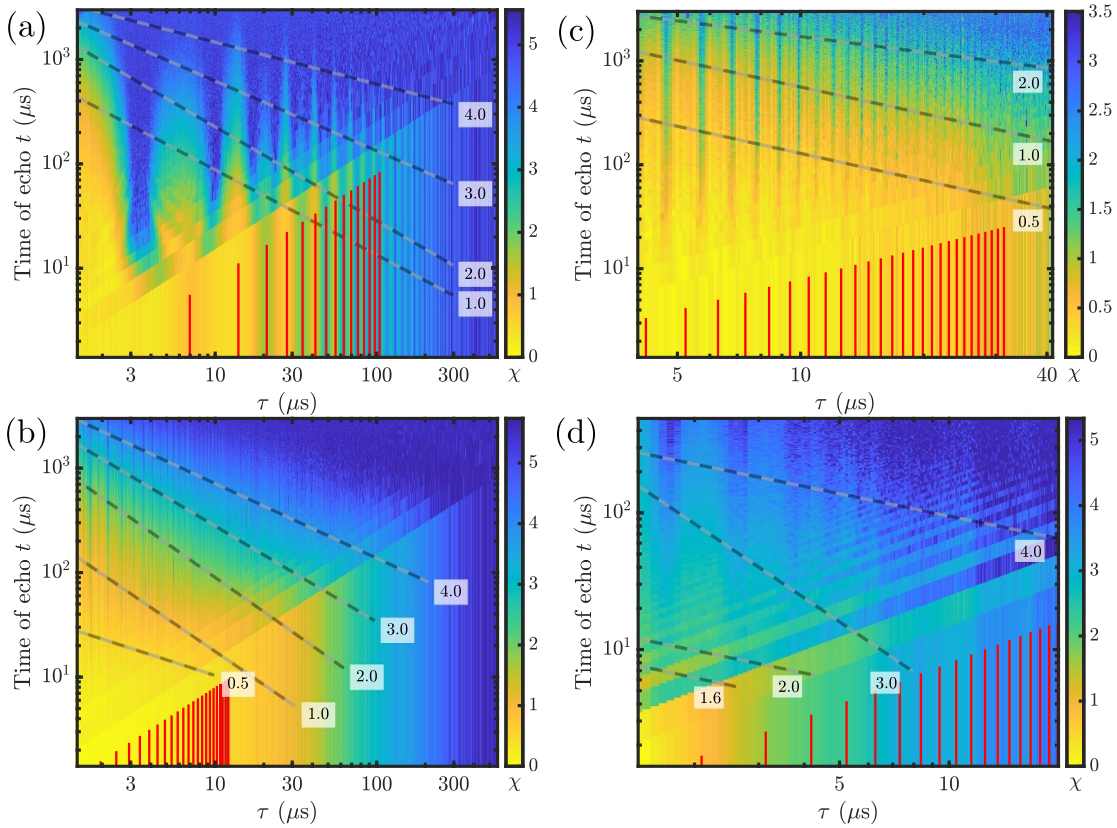

Figure 2. Image plots of χ data from CPMG experiments. (a) and (b) show data obtained with Sample A on NV centers at 13 mT and 190 mT respectively. (c) and (d) show data obtained with P1 centers at 89 mT in Samples B and A respectively. $\chi = 0$ indicates the maximum echo amplitude for the dataset. These data are T_1-corrected as described by equation (13). The broad character of the power spectrum is captured by the transparent black and white dashed lines, which are power law fits to contours of constant χ given by equation (17). The corresponding χ values are labeled at the lower right ends of the lines. The red vertical lines at the bottoms of the plots indicate τ values where coherence revivals are expected: $\tau = m\pi/\omega_{13C}$, where m is even and ω_{13C} is the ^{13}C Larmor frequency. For the 13 mT in (a), the fits are applied only to the local t maxima of the χ contours, which occur at these revival τ values.

which is all $N = 1$ (Hahn echo), with the $N = 2$ section directly above it, and so on. The image plot is constructed by defining the τ and t axes first and then populating the 2D array with χ values from the data set that most nearly match for each point (τ, t).

The χ data exhibit a combination of a broad background and sharp modulations due to electron spin echo envelope modulations (ESEEMs) arising from ^{13}C hyperfine interactions. Accordingly, our analysis involves characterization of the background spectrum S_B and the sharp peak S_P due to the ^{13}C transverse hyperfine interaction. We model the total spectrum as the sum of these contributions:

$$S(\omega) = S_B(\omega) + S_P(\omega). \tag{14}$$

The notable difference between the two NV center datasets, figures 2(a) and (b), is that the sharp ESEEM modulations dominate the 13 mT data (a). These modulations are also apparent in the 190 mT data (b) at lower τ values, but have approximately 15 times shorter periodicity in τ at the higher field. The ESEEM modulations prevent a clear measurement of S_B. However, this also means that at 13 mT, S_P can be measured directly using equation (12). To obtain the background at 13 mT, we analyze the coherence at revival τ values ($\tau = m\pi/\omega_{13C}$, where $m = 2, 4, 6\ldots$), which amounts to the standard method of fitting a decay envelope to ESEEM peak revivals [29, 38, 48]. The decay of the 13 mT CPMG data at revival τ values (indicated by the vertical red lines) is similar to the decays at 190 mT. At 190 mT, the ^{13}C modulations are more subtle, allowing a clearer characterization of S_B, which is then used in a background subtraction step to characterize S_P with higher harmonics of the CPMG filter function.

Comparing the two P1 center datasets, the decay is notably faster for the high [N] sample, figure 2(d), than the low [N] sample, figure 2(c). The P1 datasets are displayed with different axes and the ESEEM occurs with approximately the same periodicity in both despite a difference in appearance due to different τ and t ranges interrogated. The high [N] dataset of figure 2(d) exhibits a prominent rapid decay with χ going from

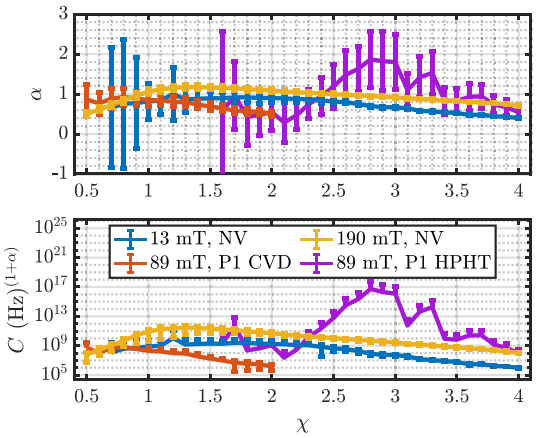

Figure 3. Parameter values from the χ contour fits for the power law model of the noise spectrum $S(\omega) = C\omega^{-\alpha}$. The error bars indicate the 95% confidence interval of the fit. See section 4.2 for further discussion.

0 to ~ 2 at early detection times, $t \lesssim 10$ μs, followed by a much more slowly decaying tail ($2 \lesssim \chi \lesssim 4$) where ESEEM is more visible. The smaller ^{13}C modulations allow a clearer characterization of S_B.

Much of our analysis focuses on the structure of fixed χ contours throughout the data sets. A commonly used approach, as in [15, 21, 58], is to focus on the contour $\chi = 1$, which is encountered when $t = T_2$, resulting in equation (12) taking the form $S(\omega_1) = \pi^2/(4T_2)$. We extend the contour tracing approach to the analysis of contours of densely sampled χ over the available range of values for two reasons. First, we find that this provides a simple way to quantitatively capture the broad character of the coherence data. Second, since larger χ values generally occur at later detection times, the δ-function approximation of the filter function has greater validity, enabling use of equations (11) and (12). This notion is consistent with the observation that longer CPMG trains lead to greater depth enhancement of the ESEEM data [24]. Conversely, in the low N limit, the peak in F is wider and is shifted from π/τ, as can be seen in figure A1(d).

Examples of the χ contour traces overlaid on a copy of figure 2 are shown in figure S6 of the supplementary information. The traces are obtained from the data as follows. For each τ, we convolve the coherence decay $\chi(t)$ with a Gaussian function: $\chi_{\text{conv}}(t) = \int_{-\infty}^{\infty} \mathrm{d}t'\, \chi(t) A \exp[-(t-t')^2/(2\sigma^2)]$, with $\sigma = 4$ μs and A being a normalization constant to preserve the magnitude of χ. This smooths out fluctuations for short τ decays and leaves longer τ decays unaffected. The χ contour is defined as the set of points (t, τ), where t for a given τ is the time of the first echo for which χ_{conv} is greater than the χ for the contour being traced.

4.2. Broad spectrum noise characterization

The dominant noise seen by a central NV or P1 center is due to the fluctuations of the surrounding P1 bath and the ^{13}C spins. Thus, the magnetic noise spectrum measured using NS of the NV and P1 centers should reflect similar underlying physics. We model the broad spectrum as a power law $S_B(\omega) = C\omega^{-\alpha}$, which enables the inclusion of harmonics that provide a small correction to the calculation of S_B [14, 21]. The discrete approximation of equation (11) becomes

$$\chi(t, \tau) = C'(\alpha)\, t\tau^{\alpha}, \tag{15}$$

where

$$C'(\alpha) = \frac{4\zeta(2+\alpha)}{\pi^{2+\alpha}} \left(1 - \frac{1}{2^{2+\alpha}}\right) C, \tag{16}$$

with ζ being the Riemann zeta function. We can find the exponent α by first rearranging equation (15) to the form

$$t = \frac{\chi(t, \tau)}{C'(\alpha)\tau^{\alpha}}. \tag{17}$$

If the noise spectrum obeys a power law of the form $S_B(\omega) = C\omega^{-\alpha}$, then, according to equation (17), a χ contour should follow a straight line on the $\log(t)$ vs $\log(\tau)$ axes. The straight black and white dashed lines in figure 2 are obtained from fitting the contours to equation (17). The fit parameters C and α from the χ contours are plotted in figure 3 and average representative values are provided in table 1.

Table 1. Average values of power law ($C\omega^{-\alpha}$) spectrum fit parameters shown in figure 3. The row labeled 'χ range' indicates the range of representative χ values used for obtaining these averages.

Sample	A	A	A	B
Species	NV	NV	P1	P1
B_0 (mT)	190	13	89	89
χ range	$0.5-4$	$1-4$	$1.6-4$	$0.5-2$
$\log_{10}(C)$	10(1)	8(2)	11(3)	8(1)
α	0.9(2)	0.7(2)	1.0(5)	0.7(2)

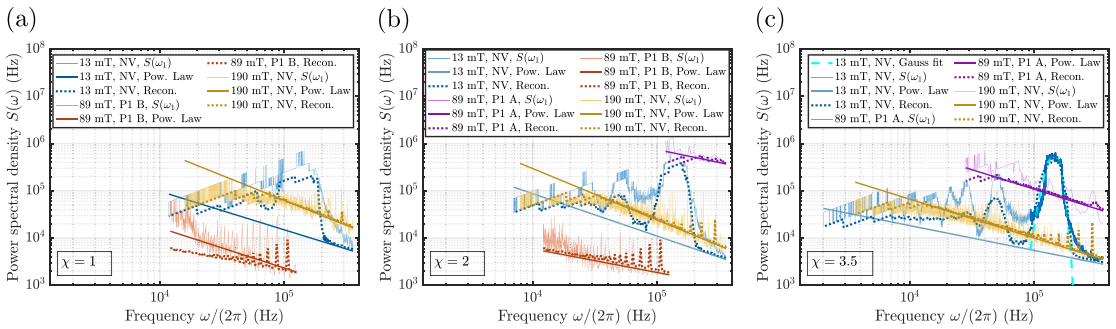

Figure 4. (a)–(c) all show spectra obtained by using equation (12) with the χ contours 1, 2 and 3.5 as indicated. The solid straight lines show the power law fits ('Pow. Law') obtained using equation (17). The reconstructed spectra ('Recon.'), which account for the deviation of the $S(\omega_1)$ data from the power law model as $\omega \to 0$, are discussed in section 4.2 and the methods of reconstruction are explained in supplementary information S6.A. Due to the contour trace consisting of experimentally realized values of detection times t, which are discrete, the low-frequency (large τ) limit of the $S(\omega_1)$ exhibits a jagged appearance, while the high-frequency (short τ) limit appears as more of a continuum. Each of the datasets exhibits subharmonics that arise due to overlap of the CPMG filter harmonics with the ^{13}C peak. Only at 13 mT is the ^{13}C peak at low enough frequency to be present in the $S(\omega_1)$ spectrum. The cyan dashed line in (c) shows the Gaussian fit to that peak.

While there is some variation in α across the measured χ values, the data suggests a frequency dependence that scales as $1/\omega^{0.7-1.0}$, as reported in table 1. The electronic spin bath surrounding an NV center has been described well by an Ornstein–Uhlenbeck (O–U) process for experiments on single NV spins in samples with low nitrogen concentration [27, 28, 30, 31, 41, 59]. The form of the power spectral density of such a process is a Lorentzian centered at $\omega = 0$,

$$S(\omega) = \frac{2\Delta^2\tau_c}{1+\omega^2\tau_c^2}, \tag{18}$$

which has a high-frequency power law tail of the form $1/\omega^2$. The origin of the scaling measured in our work being much closer to $1/\omega$ than $1/\omega^2$ is not definitely understood, but we suspect that the high concentration of nitrogen and the reported heterogeneity of the nitrogen concentration throughout the sample play significant roles [40, 50–52]. One possibility is that the high P1 concentration, which will have much stronger P1–P1 dipolar couplings and exchange couplings [51], leads to a fundamentally different type of dynamics and the O–U model no longer applies. Another possibility, motivated by [60, 61], is that the high concentration P1 baths still undergo O–U dynamics, but their correlation times τ_c vary with concentration, giving the appearance of an approximate $1/\omega$ noise in our ensemble measurement. See supplementary information S4 for further discussion. The extended CPMG decay tails of the Sample A P1 data, as well as the bi-exponential Hahn Echo decay in figure S1(e), are highly indicative of the heterogeneity of P1 concentration. Similar heterogeneity effects might explain the roughly $1/\omega$ spectrum measured with the P1 centers in Sample B, however P1 clustering has not been investigated to the same degree in CVD diamonds.

Figure 4 shows the power spectra obtained for $\chi = 1$, 2 and 3.5 using the power-law model, the approximation in equation (12), and a reconstruction technique that accounts for the finite spectrum as $\omega \to 0$. We can reliably reconstruct $S(\omega_1)$ from the power law model and a numerically computed CPMG filter function. In this case the power law model is indistinguishable from an alternative spectrum model (such as a stretched Lorentzian) that has a finite value of S at $\omega \to 0$. The details of the reconstruction are given in supplementary information S6.A, and the zero-frequency limit of the power spectra are reported in supplementary information S7.

Since the power law fits for the 13 mT dataset were applied to the local maxima of t at revival τ values, the power laws that appear in the frequency domain follow the minima between the subharmonics of the 13 mT $S(\omega_1)$ spectrum. The power laws are seen in figures 4(a)–(c) to match $S(\omega_1)$ in the mid- to

high-frequency region. At lower frequencies, particularly for the 190 mT dataset, the power law is significantly higher than the $S(\omega_1)$ data.

In figure 4, the overall lower level of the spectrum for the P1 centers in Sample B is primarily due to that sample having a much lower concentration of nitrogen [47, 48]. Comparing the 13 mT and 190 mT NV data, we see that the 13 mT spectrum dips lower than the 190 mT spectrum, indicating elevated low-frequency noise at higher field. The cause of this may be increased axial alignment of the P1 bath spins at the higher field. The ^{13}C may also play a significant role in this, since at high field, the Zeeman interaction dominates the ^{13}C Hamiltonian, but at low field the NV hyperfine interaction is comparable to or dominates the ^{13}C Hamiltonian [62].

The inhomogeneity of P1 centers in Sample A results in a range of local P1 concentrations. For regions with a high local P1 concentration, the magnetic dipolar interactions between spins are too strong for their dynamics to accurately be captured by the central spin model. However, we can still extend our analysis to the experiments on Sample A, as long as we interpret the results carefully. The rapid early decay of the Sample A P1 CPMG experiments translates to a higher level of magnetic noise power in the frequency range of dephasing noise as seen in figure 4(b) with the $\chi = 2$ contour. For $\chi < 1.6$ there were not enough data points to obtain a meaningful contour in the Sample A P1 data, and so it is omitted from figure 4(a). In the range of $1.6 \lesssim \chi \lesssim 2$, there are very few data points comprising the contour, which leads to very large error bars on the power law fit parameters in figure 3. The larger χ contours, which are traced through the tail of the decays, exhibit power spectra that are more similar to the NV power spectra. This suggests that there is a significant sub-population of P1 centers in Sample A that are more sparsely distributed.

We have also investigated experimentally and numerically how finite pulses and over/under rotation errors affect the power law characterization. These investigations are presented in supplementary information S6. We find that the finite pulses in our experiments do not significantly affect the results of the power law characterization. This is because the finite pulses most significantly affect the higher harmonics of the filter function, and in the context of a power law spectrum, these harmonics contribute only a very small amount to the χ integral in equation (7).

4.3. Characterizing the ^{13}C Larmor frequency

The transverse component of the ^{13}C hyperfine interaction contributes a peak S_{P} to the power spectrum at the ^{13}C Larmor precession frequency. We can use equation (12) to observe this peak at 13 mT. However, at 89 mT and 190 mT, the ^{13}C Larmor precession period is significantly shorter than the shortest τ we can use in our CPMG experiments, and we only see the periodic modulation of the coherence curves with increasing τ as higher harmonics of the filter function overlap with the ^{13}C peak. We have developed an analysis procedure that utilizes all applicable harmonics of the filter function to estimate the properties of S_{P} at high frequencies. The basic approach is outlined below and details are provided in appendix. Note that S_{P} could also be generalized to a sum of sharp peaks $\sum_i S_{\mathrm{P}}^i$ for contexts wherein the goal is to obtain the spectrum of a more complex system.

Inserting the composite spectrum expression of equation (14) into the discrete χ calculation of equation (11), we obtain

$$\chi(t,\tau) = \frac{4t}{\pi^2} \sum_{m=1,3,5\ldots}^{\infty} \frac{S_{\mathrm{B}}(m\pi/\tau) + S_{\mathrm{P}}(m\pi/\tau)}{m^2}. \tag{19}$$

For a sharp peak, we can assume that $S_{\mathrm{P}}(\omega) = 0$ for all m except near the sharp feature which is peaked at a frequency ω_{P}. In the vicinity of the peak we define the scanning frequency ω_s and scanning harmonic m_s with $\omega_s \equiv m_s\pi/\tau$. Then the summation of S_{P} collapses to only the $m = m_s$ term:

$$\chi(t,\tau) = \frac{4t}{\pi^2}\left[\left(\sum_{m=1,3,5\ldots}^{\infty} \frac{S_{\mathrm{B}}(m\pi/\tau)}{m^2}\right) + \frac{S_{\mathrm{P}}(\omega_s)}{m_s^2}\right]. \tag{20}$$

We solve for S_{P} and express the result as the difference between the measured χ and the background component χ_{B}, which was obtained by fitting equation (15) as described in section 4.2, resulting in

$$S_{\mathrm{P}}(\omega_s) = \frac{\pi^2 m_s^2}{4t}\left[\chi(t,\tau) - \chi_{\mathrm{B}}(t,\tau)\right]. \tag{21}$$

Figure A2 of the appendix depicts an example of this calculation. When we perform this calculation in our analysis, we include an additional term in the pre-factor to account for finite pulse widths as explained in supplementary information S6. For a given combination of τ and t, we first compute χ_{B} by determining which power law model (corresponding to the different χ contour fits) most nearly approaches the given τ

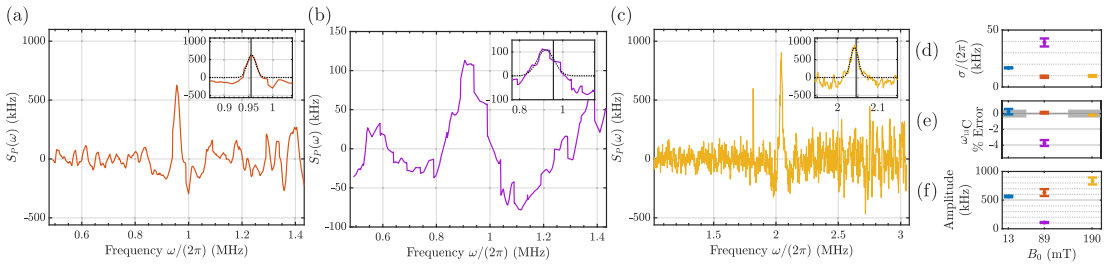

Figure 5. High-frequency spectra for (a) P1 center in Sample B at 89 mT, (b) P1 center in Sample A at 89 mT, and (c) NV center in Sample A at 190 mT. These spectra are obtained via the harmonic analysis method presented in appendix. The insets show detail of the ^{13}C peak fit to a Gaussian curve (dotted lines) and the expected ^{13}C Larmor frequency (vertical black lines). (d)–(f) show the fit parameters from applying Gaussian fits ($A\exp[-(\omega-\omega_{13C})^2]/(2\sigma^2)]$) to the ^{13}C peak, where ω_{13C} is the predicted frequency of the ^{13}C Larmor frequency based on experimental conditions. (e) shows the deviation of fit frequency from the predicted frequency, with the gray bands indicating the uncertainty of the prediction. The fits for the 89 mT and 190 mT data are those shown in the insets of (a)–(c). For the 13 mT data, the fit was applied to the $S(\omega_1)$ $\chi = 3.5$ spectrum indicated by the cyan dashed line in figure 4(c).

and t point. This is the same as determining by an image plot in figure 2, which black and white dashed line most nearly crosses a particular (t,τ) point. That power law model is then used to compute the expected value of χ_B using equation (15).

A spectrum S_P is obtained by combining the results of evaluating equation (21) for all applicable combinations of τ and t in the dataset. The procedure for this calculation is provided in appendix. The resulting spectra for the 89 mT and 190 mT data are shown in figures 5(a)–(c). We note that while negative values are not permitted in a power spectrum, they appear here because obtaining the spectra S_P via equation (21) is effectively a form of baseline subtraction.

Figures 5(d)–(f) show the fit parameters obtained from fitting a Gaussian to the reconstructed ^{13}C spectral line. The error bars indicate the 95% confidence intervals. For the 13 mT experiment, we use the $\chi = 3.5$ contour to obtain the fit. The data to which the fit is applied is the portion of $S(\omega_1)$ between 90 kHz and 200 kHz (indicated by the thicker blue line), and the fit curve is the cyan dashed line in figure 4(c). For the 89 mT and 190 mT analyses, the fit is shown in the insets of figures 5(a)–(c).

The Sample A P1 center spectrum of the ^{13}C stands out as having approximately 5× lower amplitude and 5× greater width than NV and Sample B P1 spectra, which are in fairly close agreement and agree well with similar measurements in the literature [38, 58]. Considering that both samples have natural isotopic abundance of ^{13}C and that there should be a generally identical distribution of magnetic environments for P1s and NVs in Sample A, the discrepancy indicates that the strong dipolar coupling of P1 centers in Sample A distorts the intrinsic characteristics of the spectrum. In other words, most of the P1 centers in Sample A have such strong dipolar couplings that the ^{13}C peak cannot be measured with conventional CPMG. Still though, the signature of ^{13}C is evident in the χ data for P1 Sample A in figure 2(d), particularly at later t. This exemplifies that the long-lived coherences that follow the rapid initial decay of many-spin systems [63] can sense peaks in the power spectrum. Note that the precision of the peak measurement is limited by requiring short τ values to obtain such coherences.

A detailed discussion of the variations in the measured properties of the ^{13}C peak is presented in supplementary information S5.

5. Summary and outlook

The use of ensemble pEPR NS using stroboscopic, inductively-detected measurements will expand our ability to study the properties of optically-dark spins that frequently form the bath for localized spin qubits. Here we performed DD NS of both P1 and NV centers in diamond, allowing us to directly contrast the local magnetic environments seen by these electronic spin systems. In the HPHT samples, the high concentration of P1 centers leads to a breakdown of the central spin model when measuring the P1 spins, though it remains valid when characterizing the dynamics of the NV centers.

All spectral reconstructions showed two prominent features—a broad background exhibiting a frequency dependence best approximated as $1/\omega^{0.7-1.0}$—and a narrow peak caused by the ^{13}C transverse nuclear hyperfine interaction. For the HPHT sample, we suspect that the deviation of this power-law spectrum from the expected O–U dynamics (i.e. Lorentzian spectrum with $1/\omega^2$ tail) is due to the high concentration and heterogeneity of P1 centers in the sample, which is supported by recent studies on clustering [40, 50–52]. It is unclear if this is also the case in CVD diamond. The heterogeneity of the HPHT diamond also manifested in

the presence of multiple decay timescales of the observed coherence in the P1 experiments. Finite pulse effects and flip angle errors do not greatly affect the broad spectrum characterization, but can have non-negligible effects on the characterization of sharp peaks in the power spectrum. Finite pulses make CPMG less sensitive to peaks at higher frequencies while flip angle errors can cause an asymmetric splitting of a spectral peak.

The harmonic analysis allowed us to perform more precise measurements of the ^{13}C frequency for P1 centers in CVD diamond at 89 mT and NV centers in HPHT diamond at 190 mT than could be obtained with the NV centers at 13 mT experiment. The P1 centers in the HPHT diamond had too short of coherence times to obtain as precise of a measurement, however this many-spin system exhibited weak coherences that persisted to late detection times where detection of the ^{13}C peak in the power spectrum was still achieved.

The methods presented in this work can be applied generally when CPMG is used to characterize noise. These methods applied to diamond could very directly inform strategies for quantum sensing, e.g. for performing nanoscale NMR [64] with electron spins as proxy sensors. Stroboscopic measurements of ensembles opens the door to adaptive measurement strategies such as actively varying τ to follow a particular χ contour, or using closed-loop feedback to perform adaptive quantum sensing.

Data availability statement

The data cannot be made publicly available upon publication because no suitable repository exists for hosting data in this field of study. The data that support the findings of this study are available upon reasonable request from the authors.

Acknowledgments

We thank Lorenza Viola, Bhargava Thyagarajan, Linta Joseph, and James Logan for helpful discussions. We thank Lihuang Zhu for helping design the pEPR spectrometer. We are grateful to Kevin Villegas Rosales and Yoav Romach of Quantum Machines for helping set up and program the OPX as well as helpful discussions. We thank Johan van Tol for help with diamond sample characterization that was performed at the National High Magnetic Field Laboratory in Tallahassee, FL. We thank Gajadhar Joshi and Jonathan Friedman for helpful insight on the loop-gap resonator design. We thank Dwayne Adams and Christopher Grant for help building the EPR probe and resonator. This work was partially supported by funding from the National Science Foundation under Grant CHE-2203681 and Cooperative Agreement OIA-1921199 and by the Gordon and Betty Moore Foundation by Grant GBMF12251. EQW acknowledges support of a QISE-NET Triplets Award funded by NSF award DMR-1747426.

Appendix. Harmonic analysis

Noise spectroscopy strategies such as approximating the filter function as its fundamental peak (equation (12)) to compute $S_P(\omega)$ or using Álvarez and Suter's matrix inversion method [21] enable one to measure the power spectral density up to the frequency $\omega = \pi/\tau_{\min}$, where $\tau_{\min}$ is the shortest τ one can implement with their experiment hardware. In applications of ac magnetic field sensing, it may occur that there are peaks in the power spectrum at frequencies a few times greater than $\pi/\tau_{\min}$, whose effects can still be seen in experiments in which τ is swept with a small step size. It is desirable to obtain a wide spectrum that includes these peaks, so that the peaks can be measured with sufficient contrast to the background. Frequency comb [18] and narrowband Slepian modulation techniques [65] are two possible ways to overcome the $\pi/\tau_{\min}$ limit. Higher harmonics of CPMG-type filters have also been used to estimate the magnitude of a spectral peak at a particular frequency [58]. Here we present an analysis method for obtaining a wide spectrum that reveals prominent features at frequencies greater than $\pi/\tau_{\min}$.

In essence, the harmonic analysis breaks the range of high frequencies into a series of blocks of width W, which are instances of a scanning window. For each instance of the window, equation (21) is computed for each valid combination of τ and echo number N for which a harmonic m_s of the filter function is present within the window. Each calculation gives a point in the spectrum at frequency $\omega = m_s\pi/\tau$. Interpolation and averaging are used to convert the set of calculated spectral points into one continuous spectrum. Results from this method are presented in figures 5(a)–(c) and S10(g) and (h).

In our case, the shortest interpulse delay τ that we can apply is 1.4 μs, as explained in supplementary information S3. The fundamental ($m = 1$) frequency of a CPMG filter function is $\omega = \pi/\tau$. So the highest frequency that we can fundamentally measure is $\omega \approx 360 \times 2\pi$ rad kHz, which can be seen as the maximum frequency of the spectra in figures 4(a)–(c) and S10(e). In those spectra however, the subharmonics of the ^{13}C peak are clearly visible. These subharmonics, which correspond to CPMG sequences with faster decays,

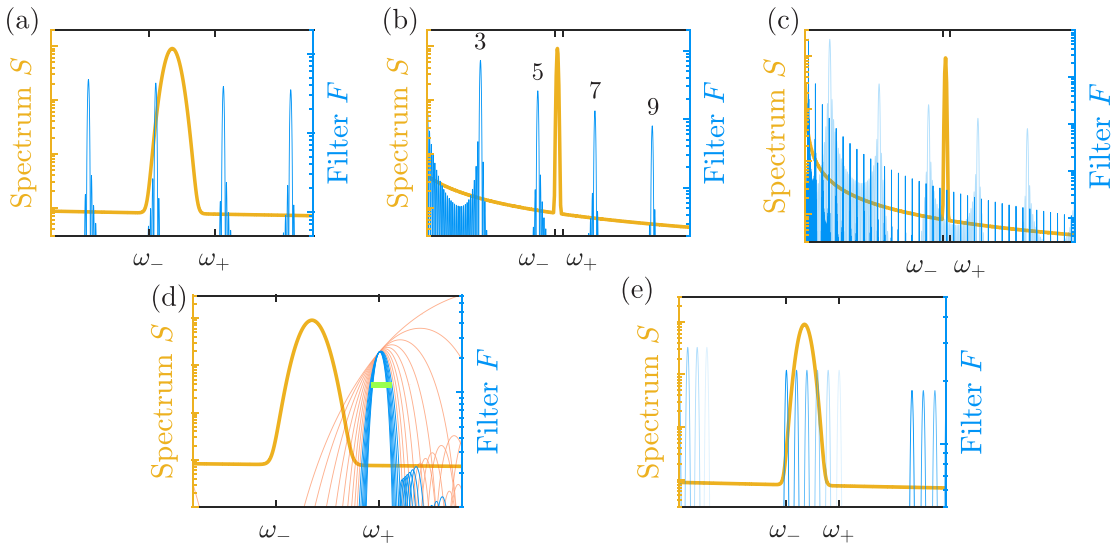

Figure A1. Illustrations of filter considerations in the harmonic analysis. See text for details.

occur at frequencies for which a higher harmonic of the filter function overlaps with the ^{13}C peak, i.e. when $\omega = \omega_{13C}/m$, where ω_{13C} is the ^{13}C nuclear Larmor frequency and m is an odd integer.

The *valid* subharmonics are ones which meet certain criteria for avoiding sensitivity limitations, avoiding distortions caused by finite widths of the peaks in the filter function, and avoiding distortions caused by multiple filter peaks overlapping with a single spectral line. These three criteria define a maximum and minimum detection time t and a maximum τ respectively. These limits can be thought of as defining a sensing region. For the 89 mT and 190 mT data analyzed in this work, the sensing regions are those indicated by the red dashed rectangles in figures A3(a), A4(a) and A5(a). The criteria for avoiding sensitivity and distortion limitations inform the following 6-step analysis protocol. Steps 1 through 5 explain the frequency scan procedure over one instance of the window, focusing on an example where the window contains a prominent peak, as depicted by the cartoon examples in figure A1. Step 6 explains how to iterate this procedure to obtain a wide spectrum.

1. Determine the width W of the frequency-scanning window. W is determined by the requirement that only one harmonic of the filter function overlap with the peak. This is the assumption that allows the isolation of S_P from the summation in equation (20). W is the maximum peak width that can be resolved by the analysis process. W sets the maximum τ value that will contribute to the calculation as $\tau_{max} = 2\pi/W$. The center of the scan window is denoted ω_c, and the upper $(+)$ and lower $(-)$ bounds of the window are $\omega_\pm = \omega_c \pm W/2$. With $\tau \leqslant \tau_{max}$, the minimum frequency difference between two consecutive peaks of the filter function is greater than or equal to W, as depicted in figure A1(a). We note that in some systems τ_{max} may be limited by a hardware or coherence limit, in which case W should be defined from τ_{max}.

2. Determine the range of harmonics, i.e. peaks of the filter F, that can be used as the scanning harmonic m_s (where m_s can be odd integers in reference to m of equation (11)). For m_{min} we want the lowest filter peak available. With the shortest τ that can be applied with the hardware, m_{min} is the lowest peak that can still reach ω_+. For the example in figure A1(b), which shows the filter for CPMG with τ_{min}, we get $m_{min} = 7$ because the $m = 5$ peak falls short of ω_+. Formally, m_{min} is the lowest odd integer greater than $\omega_+\tau_{min}/\pi$. As τ increases, the peaks in F contract toward 0. The maximum harmonic m_{max} is then determined by requiring that only one harmonic can be in the range $[\omega_-, \omega_+]$. Specifically, when the m_{max} peak is at $\omega_- = \pi\, m_{max}/\tau_{max}$, the $m_{max} + 2$ peak should be at a frequency greater than ω_+:

$$\frac{(m_{max} + 2)\,\pi}{\tau_{max}} \geqslant \omega_- + W. \tag{A.1}$$

This inequality is more succinctly expressed in terms of W. We say that m_{max} is the highest odd integer subject to the constraint

$$m_{max} \leqslant \frac{2\omega_-}{W}. \tag{A.2}$$

Figure A1(c) shows the filters for τ_{min} (light blue) and τ_{max} (darker blue).

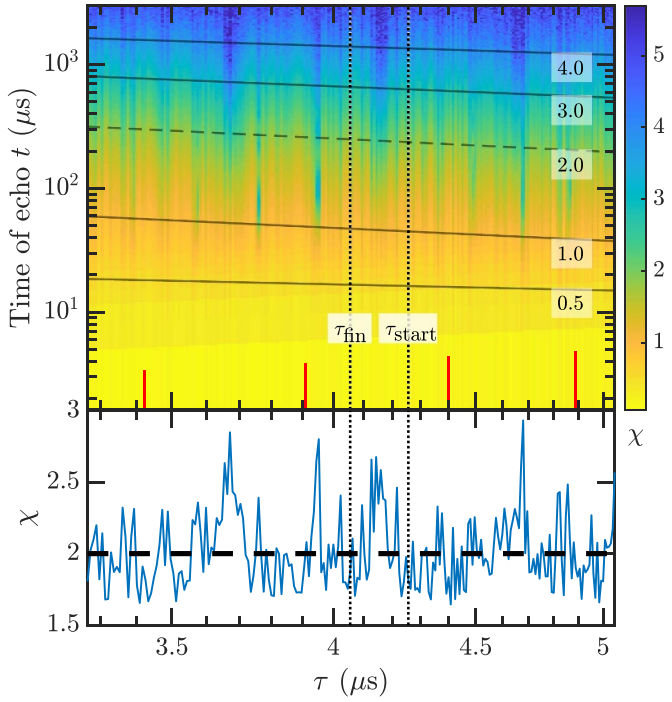

Figure A2. Example of the background subtraction (equation (21)) in the harmonic analysis. The top plot shows a zoomed in section of the image coherence plot of the 190 mT NV data shown in figure 2(b). The bottom plot shows the value of χ along the $\chi = 2$ power law fit line (dashed line). This figure serves as a visual example of the ^{13}C peak S_{P} calculation described in Step 5 of the harmonic analysis.

3. For a given scan harmonic m_s determine the starting and finishing τ values to iterate over. Assuming we are sweeping m_s in the direction of increasing ω (as inferred by the increasing transparency of the blue peaks in figure A1(e)), then the τ values are swept in decreasing order, $\tau_{\text{start}} > \tau_{\text{fin}}$ (see the example in figure A2). The corresponding frequencies $\omega_{\text{start}} = m_s\pi/\tau_{\text{start}}$ and $\omega_{\text{fin}} = m_s\pi/\tau_{\text{fin}}$ will not necessarily be equal to ω_- and ω_+. Rather, ω_{start} and ω_{fin} should be within the bounds of ω_- and ω_+.

$$\omega_{\text{start}} \geqslant \omega_- \tag{A.3}$$

$$\frac{m_s\pi}{\tau_{\text{start}}} \geqslant \omega_- \tag{A.4}$$

$$\tau_{\text{start}} \leqslant \frac{m_s\pi}{\omega_-}. \tag{A.5}$$

τ_{start} is the highest available τ subject to this constraint. Similarly,

$$\omega_{\text{fin}} \leqslant \omega_+ \tag{A.6}$$

$$\frac{m_s\pi}{\tau_{\text{fin}}} \leqslant \omega_+ \tag{A.7}$$

$$\tau_{\text{fin}} \geqslant \frac{\pi\, m_s}{\omega_+}. \tag{A.8}$$

τ_{fin} is the lowest available τ subject to this constraint.

4. For a given m_s and associated range $[\tau_{\text{fin}}, \tau_{\text{start}}]$, determine the range of echo numbers $[N_{\text{min}}, N_{\text{max}}]$. To determine N_{min}, it must be taken into account that the peaks in the filter function F have finite width, which becomes narrower with increasing N. Therefore, N_{min} should be set by requiring that the harmonic peak is narrower than the sharp peak needing to be resolved. Without knowing the sharp peak's width beforehand, one can instead require that the harmonic peak width be much narrower than the scan frequency range W. With $\sigma = \sqrt{2\pi}/(N\tau)$ being the width of the scan harmonic peak (obtained from the Gaussian approximation of the peaks in the filter F [57]), we require $\sigma < \epsilon W$, with $\epsilon \ll 1$. This leads to

$$N_{\text{min}} > \frac{\sqrt{2\pi}}{\epsilon W \tau_{\text{fin}}}. \tag{A.9}$$

N_{min} is the lowest N available subject to this constraint. In figure A1(d), filters are shown for a fixed τ and $N = 1$ through 16. The horizontal green bar has width $2\epsilon W$. The red filters are $1 \leqslant N \leqslant 9$ and fail the width

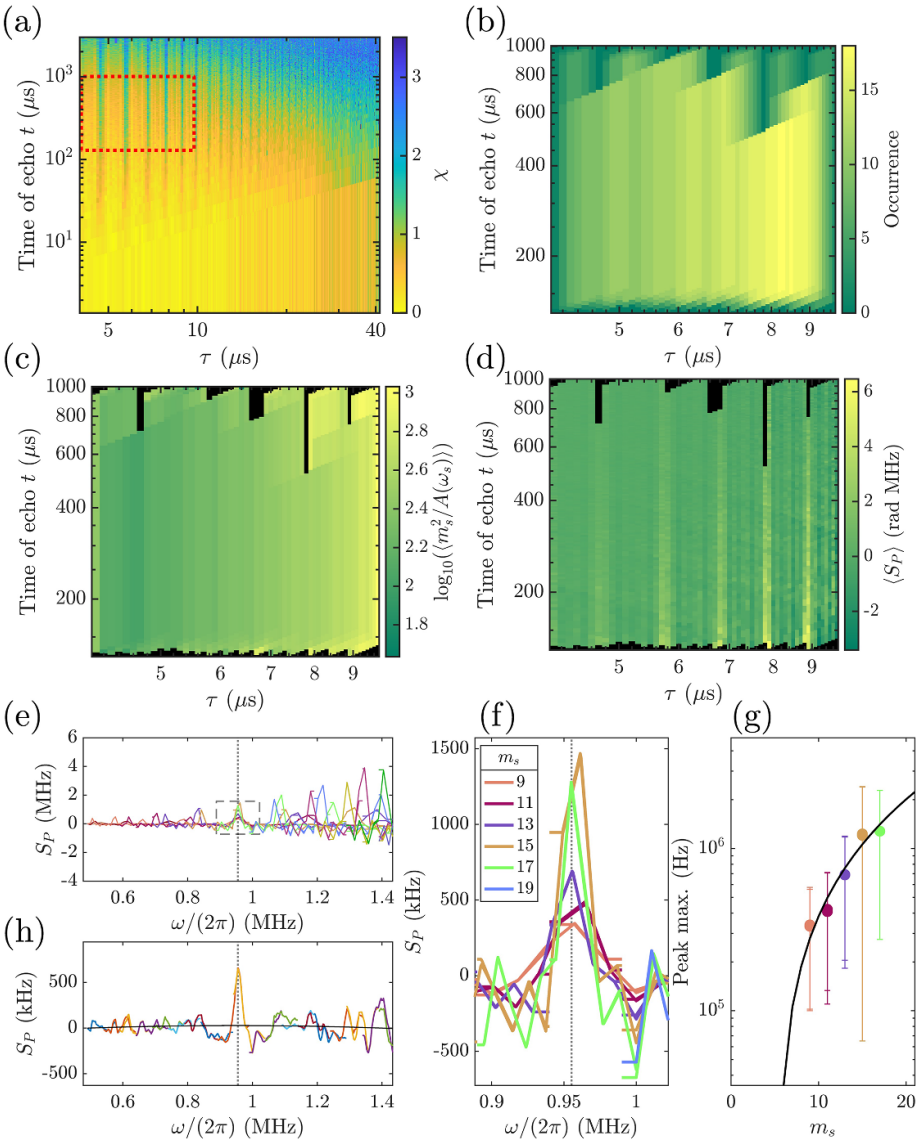

Figure A3. Visualizations of parts of the harmonic analysis procedure for the 89 mT P1 Sample B data. (a) Image plot of the coherence data. The red dashed rectangle indicates the 'sensing region' over which it is valid to use the δ approximation of the filter function to characterize the ^{13}C peak. This is the region that plots (b)–(d) show. (b) Number of times each point of the data is used in the harmonic analysis. (c) Log_{10} of the average harmonic weighting prefactor in the calculation of equation (21). $A(\omega_s)$ is the finite filter correction explained in supplementary information S6.A. (d) Average contribution of each data point in the calculation of S_P in the harmonic analysis. (e) Spectral segments described in Steps 5 and 6 of the harmonic analysis. A segment is obtained using one harmonic m_s and averaged over all available N. The vertical gray dotted line represents the ^{13}C Larmor frequency. (f) Detail of the area outlined by the gray dashed box in (e) with the legend indicating which filter harmonic each segment was obtained with. (g) Maxima of the peaks shown in (f). The black line is a quadratic fit. See supplementary information S5 for discussion. (h) Overlapping segments of width W obtained when averaging the contributions from all available harmonics as discussed in Steps 5 and 6 of the harmonic analysis. These are then averaged to produce the spectrum in figure 5(a).

criterion. The blue filters are $10 \leqslant N \leqslant 16$ and satisfy the width criterion. N_{max} should be determined by some SNR threshold or T_1 limit. We use $N_{\text{max}}\tau_{\text{start}} < 1$ ms, which is sufficiently shorter than the 2 ms T_1 of the P1 center. Note, in the definitions of N_{min} and N_{max}, we have inserted τ_{fin} and τ_{start} respectively, to place the more restrictive constraints on the N range. This ensures that the N range meets the requirements for the entire τ range and the given m_s. Since the detection time is $t = N\tau$, these width limits set a maximum and minimum t, which are the tops and bottoms of the red dashed rectangles in (a) of figures A3–A5.

5. Compute $S_{\text{P}}(m_s\pi/\tau)$ using equation (21). For each combination of m_s and N, a segment of the spectrum $S_{\text{P}}(\omega)$ is obtained by sweeping τ from τ_{start} to τ_{fin}. These segments are averaged over the available N (seen in (e) and (f) of figures A3–A5). Then each of those segments is averaged over the available m_s resulting in a single segment seen in (h) of figures A3–A5. Figure A2 provides example data from the 190 mT experiment to illustrate how equation (21) is calculated. The effective bounds of the scanning window represented in the τ-domain by τ_{start} and τ_{fin} are indicated by the vertical dotted lines. In the middle of this window, we see more rapid decay due to a filter harmonic overlapping with the ^{13}C peak. $\chi(t,\tau)$ is the exact

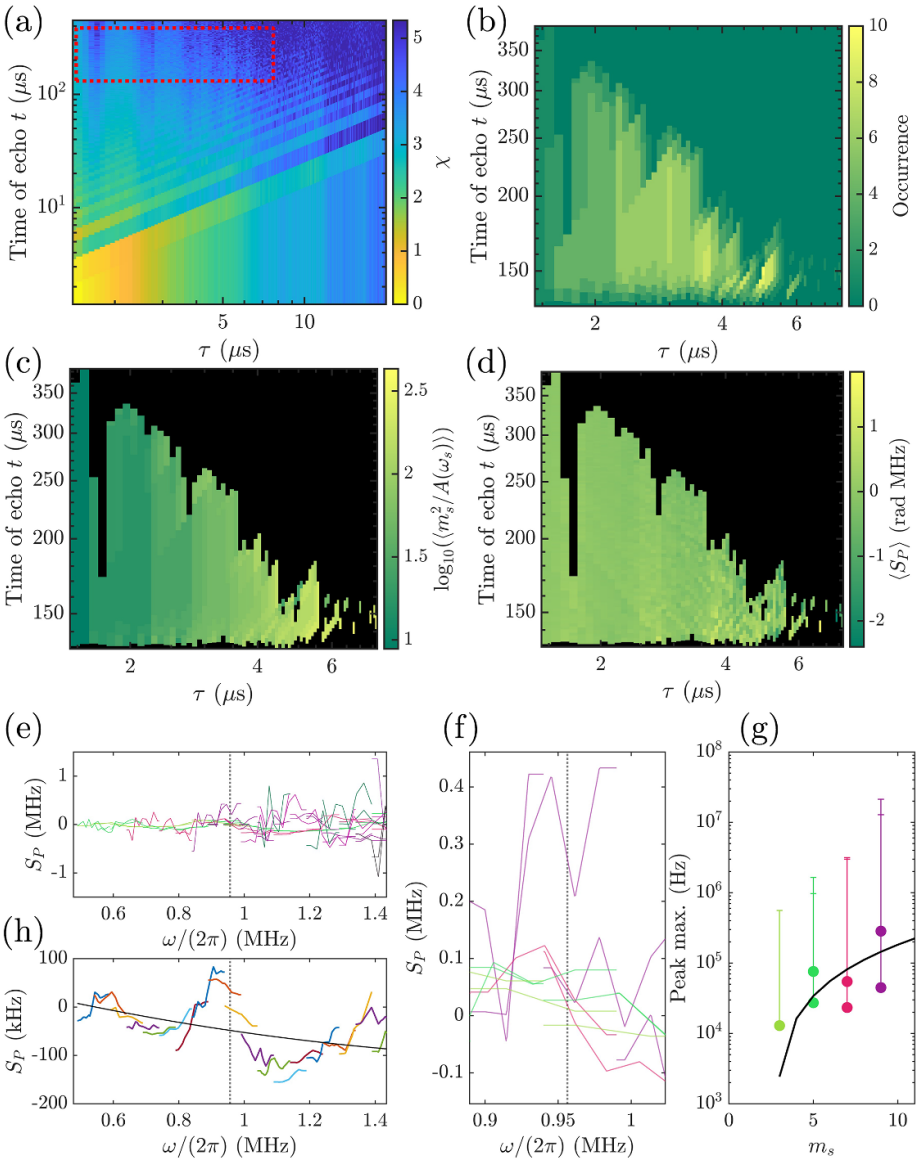

Figure A4. Visualizations of parts of the harmonic analysis procedure for the 89 mT P1 Sample A data. See the caption to figure A3 for descriptions. The averaged segments in (h) are averaged to produce the spectrum in figure 5(b).

value of χ at the point in question. To determine χ_B for a given combination of τ and N, we determine which χ contour fit (straight black lines) most closely crosses over that point, and use the parameters from that fit to calculate the precise value of χ_B. We solve equation (15) for the various χ contour characterizations, and find which χ contour fit predicts the closest N to the point in question with the given τ. For example, the point at $\tau = 4.15$ μs and $t = N\tau = 230$ μs has the $\chi = 2$ contour fit (dashed line) crossing over it, so $\chi_B = 2$ for that point. The lower plot in figure A2 shows the value of the measured χ along the power law fit of the $\chi = 2$ contour. So the subtraction term in brackets of equation (21) is $\chi - \chi_B = 2.5 - 2 = 0.5$. In experiments, it may be the case that τ is sampled linearly with hardware-limited precision. Therefore, the spectrum of $S_P(\omega)$ has $1/\omega$ sampling. The array of S_P values can be resampled, using interpolation, onto a linearly spaced array of ω values with a small step size to create a segment of the spectrum. The linearly resampled spectrum segments can then be added together for each combination of m_s and τ for averaging.

6. Perform Steps 1–5 for a wide sweep of the window position ω_c, while maintaining the fixed window width W. The spectral segments of adjacent ranges $[\omega_-, \omega_+]$ can then be stitched together in order to generate the spectrum over a wide frequency range. Furthermore, to average out interpolation artifacts that may arise at the edges of the scanning window, one can overlap the ranges such that any range starts at $W/2$ greater than the ω_- of the previous range as in a bricklaying pattern as in (h) of figures A3–A5.

Figures A3–A5 show intermediate steps of the harmonic analysis for the P1 data at 89 mT and NV data at 190 mT. The plots (a) of figures A3–A5 indicate the valid sensing region with the red dashed rectangles. We

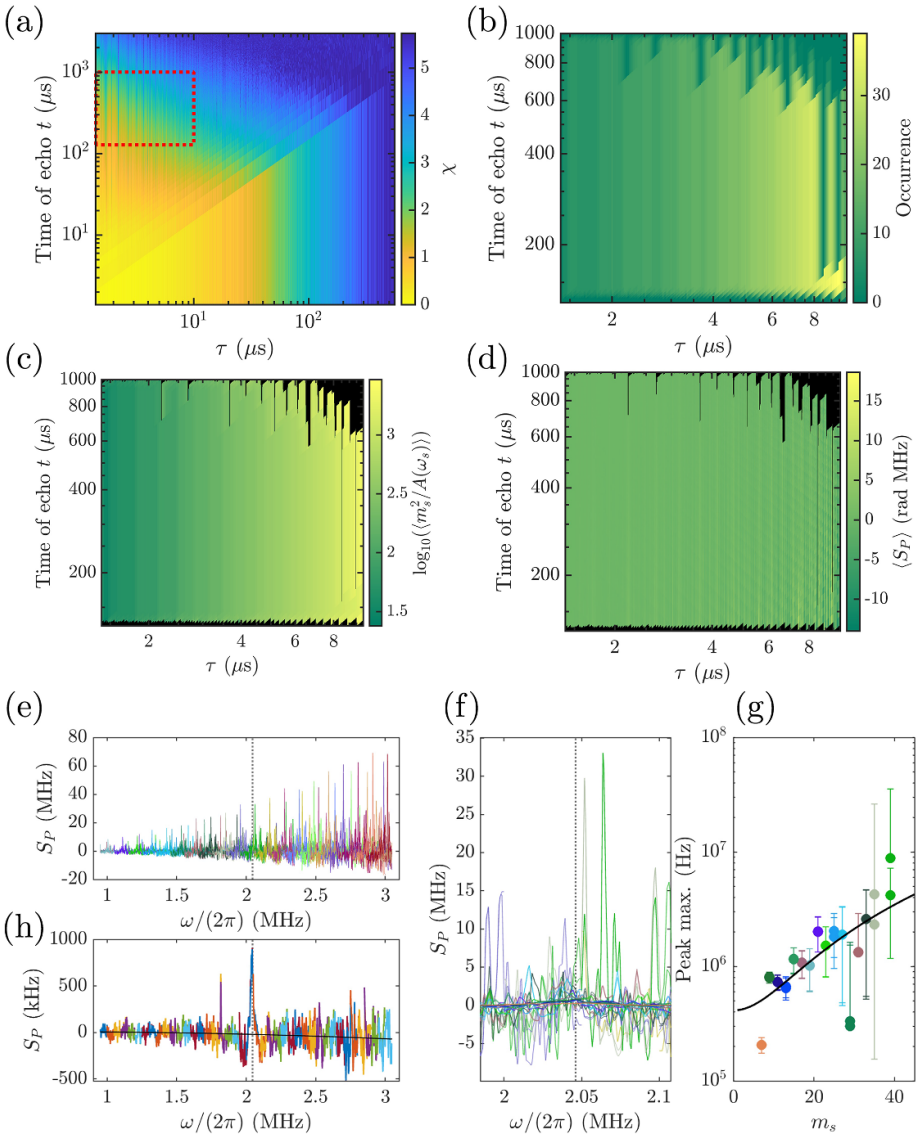

Figure A5. Visualizations of parts of the harmonic analysis procedure for the 190 mT NV data. See the caption to figure A3 for descriptions. (f) Does not include a legend as in figure A3 because the spectral segments are too dense to separately distinguish. The averaged segments in (h) are averaged to produce the spectrum in figure 5(c).

set the maximum detection time t to be 1 ms for the P1 Sample A and NV data, and 450 μs for the P1 Sample B data, to stay well within T_1 relaxation limitations. We set the maximum $\tau_{\max} \leqslant 10$ μs, which gives $W = 2\pi \times 100$ rad kHz, approximately 5 times wider than the width (2σ) of the ^{13}C peak. We set $W\epsilon = 2\pi \times 3$ kHz, which is sufficiently narrower than the ^{13}C peak and corresponds to a minimum detection time of $t \approx 133$ μs. Figures (b)–(d) of A3–A5 reveal how each data point in the sensing region is incorporated into the harmonic analysis. The (b) figures simply show how many times each point was used in the calculation of equation (21). In order to avoid the sensitivity limits of decoherence, points were omitted if the χ value was greater than a noise threshold: 2 for the Sample B data and 4.5 for the Sample A data.

ORCID iDs

Ethan Q Williams https://orcid.org/0000-0001-5672-5383
Chandrasekhar Ramanathan https://orcid.org/0000-0002-7457-3608

References

[1] Zu C *et al* 2021 Emergent hydrodynamics in a strongly interacting dipolar spin ensemble *Nature* **597** 45–50
[2] Davis E J *et al* 2023 Probing many-body dynamics in a two-dimensional dipolar spin ensemble *Nat. Phys.* **19** 836–44
[3] Goldblatt R M, Martin A M and Wood A A 2024 Sensing coherent nuclear spin dynamics with an ensemble of paramagnetic nitrogen spins *PRX Quantum* **5** 020334

[4] Degen M J, Loenen S J H, Bartling H P, Bradley C E, Meinsma A L, Markham M, Twitchen D J and Taminiau T H 2021 Entanglement of dark electron-nuclear spin defects in diamond *Nat. Commun.* **12** 3470
[5] Gaita-Ariño A, Luis F, Hill S and Coronado E 2019 Molecular spins for quantum computation *Nat. Chem.* **11** 301–9
[6] Chilton. N F 2022 Molecular magnetism *Annu. Rev. Mater. Res.* **52** 79–101
[7] Wu Y, Zhou J, Nelson J N, Young R M, Krzyaniak M D and Wasielewski M R 2018 Covalent radical pairs as spin qubits: influence of rapid electron motion between two equivalent sites on spin coherence *J. Am. Chem. Soc.* **140** 13011–21
[8] Fataftah M S *et al* 2020 Trigonal bipyramidal V3+ complex as an optically addressable molecular qubit candidate *J. Am. Chem. Soc.* **142** 20400–8
[9] Jellen M J, Ayodele M J, Cantu A, Forbes M D E and Garcia-Garibay M A 2020 2D arrays of organic qubit candidates embedded into a pillared-paddlewheel metal–organic framework *J. Am. Chem. Soc.* **142** 18513–21
[10] Carr H Y and Purcell E M 1954 Effects of diffusion on free precession in nuclear magnetic resonance experiments *Phys. Rev.* **94** 630–8
[11] Meiboom S and Gill D 1958 Modified spin-echo method for measuring nuclear relaxation times *Rev. Sci. Instrum.* **29** 688–91
[12] Viola L, Knill E and Lloyd S 1999 Dynamical decoupling of open quantum systems *Phys. Rev. Lett.* **82** 2417–21
[13] Uhrig G S 2007 Keeping a quantum bit alive by optimized π-pulse sequences *Phys. Rev. Lett.* **98** 100504
[14] Cywiński L, Lutchyn R M, Nave C P and Das Sarma S 2008 How to enhance dephasing time in superconducting qubits *Phys. Rev.* B **77** 174509
[15] Yuge T, Sasaki S and Hirayama Y 2011 Measurement of the noise spectrum using a multiple-pulse sequence *Phys. Rev. Lett.* **107** 170504
[16] Biercuk M J, Doherty A C and Uys H 2011 Dynamical decoupling sequence construction as a filter-design problem *J. Phys. B: At. Mol. Opt. Phys.* **44** 154002
[17] Pham L M, Bar-Gill N, Belthangady C, Le Sage D, Cappellaro P, Lukin M D, Yacoby A and Walsworth R L 2012 Enhanced solid-state multispin metrology using dynamical decoupling *Phys. Rev.* B **86** 045214
[18] Norris L M, Paz-Silva G A and Viola L 2016 Qubit noise spectroscopy for non-gaussian dephasing environments *Phys. Rev. Lett.* **116** 150503
[19] Degen C L, Reinhard F and Cappellaro P 2017 Quantum sensing *Rev. Mod. Phys.* **89** 035002
[20] Ajoy A, Álvarez G A and Suter D 2011 Optimal pulse spacing for dynamical decoupling in the presence of a purely dephasing spin bath *Phys. Rev.* A **83** 032303
[21] Álvarez G A and Suter D 2011 Measuring the spectrum of colored noise by dynamical decoupling *Phys. Rev. Lett.* **107** 230501
[22] Harbridge J R, Eaton S S and Eaton G R 2003 Comparison of electron spin relaxation times measured by Carr–Purcell–Meiboom–Gill and two-pulse spin-echo sequences *J. Magn. Reson.* **164** 44–53
[23] Mitrikas G, Efthimiadou E K and Kordas G 2014 Extending the electron spin coherence time of atomic hydrogen by dynamical decoupling *Phys. Chem. Chem. Phys.* **16** 2378–83
[24] Mitrikas G and Prokopiou G 2015 Modulation depth enhancement of ESEEM experiments using pulse trains *J. Magn. Reson.* **254** 75–85
[25] Fu Y, Wu Y, Dai Y, Qin Xi, Rong X and Du J 2021 Molecular-spin-qubit noise spectroscopy through dynamical decoupling *Phys. Rev. Appl.* **15** L061001
[26] Bylander J, Gustavsson S, Yan F, Yoshihara F, Harrabi K, Fitch G, Cory D G, Nakamura Y, Tsai J-S and Oliver W D 2011 Noise spectroscopy through dynamical decoupling with a superconducting flux qubit *Nat. Phys.* **7** 565–70
[27] Sung Y *et al* 2019 Non-Gaussian noise spectroscopy with a superconducting qubit sensor *Nat. Commun.* **10** 3715
[28] de Lange G, Wang Z H, Ristè D, Dobrovitski V V and Hanson R 2010 Universal dynamical decoupling of a single solid-state spin from a spin bath *Science* **330** 60–63
[29] Ryan C A, Hodges J S and Cory D G 2010 Robust decoupling techniques to extend quantum coherence in diamond *Phys. Rev. Lett.* **105** 200402
[30] Bar-Gill N, Pham L M, Belthangady C, Le Sage D, Cappellaro P, Maze J R, Lukin M D, Yacoby A and Walsworth R 2012 Suppression of spin-bath dynamics for improved coherence of multi-spin-qubit systems *Nat. Commun.* **3** 858
[31] Wang Z-H and Takahashi S 2013 Spin decoherence and electron spin bath noise of a nitrogen-vacancy center in diamond *Phys. Rev.* B **87** 115122
[32] Staudacher T, Shi F, Pezzagna S, Meijer J, Du J, Meriles C A, Reinhard F and Wrachtrup J 2013 Nuclear magnetic resonance spectroscopy on a (5-nanometer)3 sample volume *Science* **339** 561–3
[33] Rosskopf T, Dussaux A, Ohashi K, Loretz M, Schirhagl R, Watanabe H, Shikata S, Itoh K M and Degen C L 2014 Investigation of surface magnetic noise by shallow spins in diamond *Phys. Rev. Lett.* **112** 147602
[34] Myers B A, Das A, Dartiailh M C, Ohno K, Awschalom D D and Bleszynski Jayich A C 2014 Probing surface noise with depth-calibrated spins in diamond *Phys. Rev. Lett.* **113** 027602
[35] Zhao N, Wrachtrup J and Liu R-B 2014 Dynamical decoupling design for identifying weakly coupled nuclear spins in a bath *Phys. Rev.* A **90** 032319
[36] Loretz M, Boss J M, Rosskopf T, Mamin H J, Rugar D and Degen C L 2015 Spurious harmonic response of multipulse quantum sensing sequences *Phys. Rev.* X **5** 021009
[37] Lang J E, Casanova J, Wang Z-Y, Plenio M B and Monteiro T S 2017 Enhanced resolution in nanoscale NMR via quantum sensing with pulses of finite duration *Phys. Rev. Appl.* **7** 054009
[38] Romach Y, Lazariev A, Avrahami I, Kleißler F, Arroyo-Camejo S and Bar-Gill N 2019 Measuring environmental quantum noise exhibiting a nonmonotonic spectral shape *Phys. Rev. Appl.* **11** 014064
[39] Smits J, Damron J T, Kehayias P, McDowell A F, Mosavian N, Fescenko I, Ristoff N, Laraoui A, Jarmola A and Acosta V M 2019 Two-dimensional nuclear magnetic resonance spectroscopy with a microfluidic diamond quantum sensor *Sci. Adv.* **5** eaaw7895
[40] Li S *et al* 2021 Determination of local defect density in diamond by double electron-electron resonance *Phys. Rev.* B **104** 094307
[41] Kyu Calvin Sun W and Cappellaro P 2022 Self-consistent noise characterization of quantum devices *Phys. Rev.* B **106** 155413
[42] Silani Y *et al* 2023 Nuclear quadrupole resonance spectroscopy with a femtotesla diamond magnetometer *Sci. Adv.* **9** eadh3189
[43] de Lange G, van der Sar T, Blok M, Wang Z-H, Dobrovitski V and Hanson R 2012 Controlling the quantum dynamics of a mesoscopic spin bath in diamond *Sci. Rep.* **2** 1–5
[44] Bauch E, Hart C A, Schloss J M, Turner M J, Barry J F, Kehayias P, Singh S and Walsworth R L 2018 Ultralong dephasing times in solid-state spin ensembles via quantum control *Phys. Rev.* X **8** 031025
[45] Artzi Y, Twig Y and Blank A 2015 Induction-detection electron spin resonance with spin sensitivity of a few tens of spins *Appl. Phys. Lett.* **106** 084104

[46] Blank A, Twig Y and Ishay Y 2017 Recent trends in high spin sensitivity magnetic resonance *J. Magn. Reson.* **280** 20–29
[47] van Wyk J A, Reynhardt E C, High G L and Kiflawi I 1997 The dependences of ESR line widths and spin - spin relaxation times of single nitrogen defects on the concentration of nitrogen defects in diamond *J. Phys. D: Appl. Phys.* **30** 1790–3
[48] Bauch E *et al* 2020 Decoherence of ensembles of nitrogen-vacancy centers in diamond *Phys. Rev.* B **102** 134210
[49] Barry J F, Schloss J M, Bauch E, Turner M J, Hart C A, Pham L M and Walsworth R L 2020 Sensitivity optimization for NV-diamond magnetometry *Rev. Mod. Phys.* **92** 015004
[50] Bussandri S, Shimon D, Equbal A, Ren Y, Takahashi S, Ramanathan C and Han S 2023 P1 center electron spin clusters are prevalent in type Ib diamonds *J. Am. Chem. Soc.* **146** 5088–99
[51] Nir-Arad O, Shlomi D H, Manukovsky N, Laster E and Kaminker I 2023 Nitrogen substitutions aggregation and clustering in diamonds as revealed by high-field electron paramagnetic resonance *J. Am. Chem. Soc.* **146** 5100–7
[52] Shimon D, Cantwell K A, Joseph L, Williams E Q, Peng Z, Takahashi S and Ramanathan C 2022 Large room temperature bulk DNP of 13C via P1 centers in diamond *J. Phys. Chem.* C **126** 17777–87
[53] Hardy W N and Whitehead L A 1981 Split-ring resonator for use in magnetic resonance from 200–2000 MHz *Rev. Sci. Instrum.* **52** 213–6
[54] Froncisz W and Hyde J S 1982 The loop-gap resonator: a new microwave lumped circuit ESR sample structure *J. Magn. Reson.* **47** 515–21
[55] Joshi G, Kubasek J, Nikolov I, Sheehan B, Costa T A, Allão Cassaro R A and Friedman. J R 2020 Adjustable coupling and in situ variable frequency electron paramagnetic resonance probe with loop-gap resonators for spectroscopy up to X-band *Rev. Sci. Instrum.* **91** 023104
[56] Smith W V, Sorokin P P, Gelles I L and Lasher G J 1959 Electron-spin resonance of nitrogen donors in diamond *Phys. Rev.* **115** 1546–52
[57] Yang W, Ma W-L and Liu R-B 2016 Quantum many-body theory for electron spin decoherence in nanoscale nuclear spin baths *Rep. Prog. Phys.* **80** 016001
[58] Hernández-Gómez S, Poggiali F, Cappellaro P and Fabbri N 2018 Noise spectroscopy of a quantum-classical environment with a diamond qubit *Phys. Rev.* B **98** 214307
[59] Romach Y *et al* 2015 Spectroscopy of surface-induced noise using shallow spins in diamond *Phys. Rev. Lett.* **114** 017601
[60] Dutta P and Horn P M 1981 Low-frequency fluctuations in solids: $\frac{1}{f}$ noise *Rev. Mod. Phys.* **53** 497–516
[61] Schriefl J, Makhlin Y, Shnirman A and Schön G 2006 Decoherence from ensembles of two-level fluctuators *New J. Phys.* **8** 1
[62] Reinhard F *et al* 2012 Tuning a spin bath through the quantum-classical transition *Phys. Rev. Lett.* **108** 200402
[63] Hahn W and Dobrovitski V V 2021 Long-lived coherence in driven many-spin systems: From two to infinite spatial dimensions *New J. Phys.* **23** 073029
[64] Schwartz I, Rosskopf J, Schmitt S, Tratzmiller B, Chen Q, McGuinness L P, Jelezko F and Plenio M B 2019 Blueprint for nanoscale NMR *Sci. Rep.* **9** 6938
[65] Frey V, Norris L M, Viola L and Biercuk M J 2020 Simultaneous spectral estimation of dephasing and amplitude noise on a qubit sensor via optimally band-limited control *Phys. Rev. Appl.* **14** 024021